J. of Intell. Mat. Sys. and Struc., Vol. 9, No. 5 pp. 379-390 (1998)

Transformation of Embedded Shape Memory Alloy Ribbons

K.D. JONNALAGADDA and N.R. SOTTOS*

Theoretical and Applied Mechanics Department, University of Illinois at Urbana-Champaign, 216 Talbot Lab, 104 S. Wright St, Urbana 61801

M.A. QIDWAI AND D.C. LAGOUDAS

Center for Mechanics of Composites, Aerospace Engineering Department, Texas A & M University, College Station TX 77843

ABSTRACT

Shape memory alloy (SMA) wires can be embedded in a host material to alter the stiffness or modal response and provide vibration control. The interaction between the embedded SMA and the host material is critical to applications requiring transfer of loads or strain from the wire to the host. Although there has been a significant amount of research dedicated to characterizing and modeling the response of SMA alone, little research has focused on the transformation behavior of embedded SMAs. In the current work, photoelasticity was used to quantify the internal stresses induced by the actuation of a thin SMA ribbon in a polymer matrix. Through the use of a CCD camera and a frame grabber, photoelastic fringes were digitally recorded at discrete time increments. The stress contours were then analyzed quantitatively as a function of time. A numerical simulation of the embedded ribbon was also carried out using a coupled SMA constitutive model. The thermomechanical model accurately predicted the stress contours throughout the experiment.

Keywords: Shape memory alloys, phase transformation, composites, photoelasticity

1. INTRODUCTION

Shape memory alloys (SMA) have been proposed as large strain actuators for use in smart structures. SMAs in the form of wires or thin films can be embedded in a host material to form a SMA composite. The potential applications of embedded SMA actuators include controlling external shape, changing stiffness and providing vibration control of the composite. There has been considerable interest in the area of SMA composites though manufacturing and processing difficulties have hampered progress. Initial attempts by Liang, Jia and Rogers (1989) and Rogers (1990) to embed Nitinol wires into polymers proved largely unsuccessful due to poor interfacial

*To whom correspondence should be addressed.

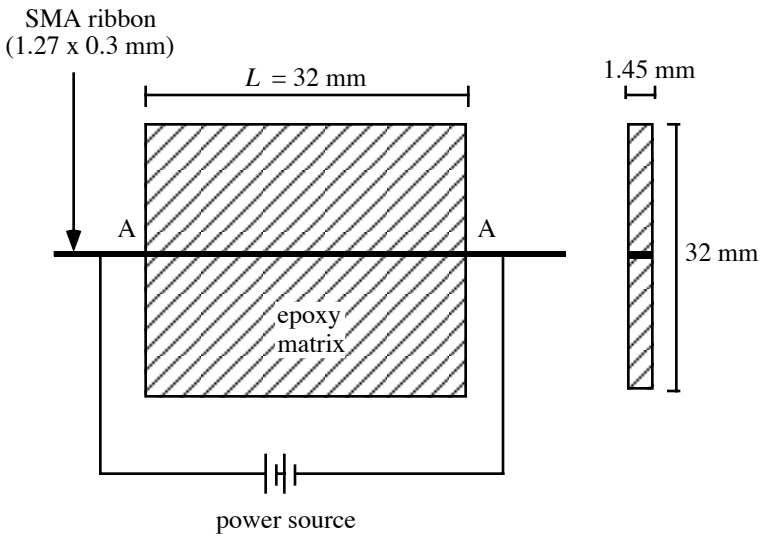

Figure 1. Schematic of SMA ribbon sample.

bonding. Subsequently, Baz and Ro (1992) and Chaudry and Rogers (1989) incorporated SMA wires using coupling sleeves and mechanical fasteners, respectively. Paine and Rogers (1991) studied the effects of processing on the performance of SMA actuators in composites. Hebda and White (1995) and Hebda, Whitlock, Ditman and White (1995) examined issues in the manufacturing of composites such as void content and the SMA wire training effects.

Although there has been a significant amount of research dedicated to characterizing and modeling the response of SMAs alone, little work has been done to understand the constitutive behavior of SMAs embedded in composites. The interaction between the embedded SMA and the host material is critical since most applications require transfer of load or strain from the wire to the host. In addition, the host material can have a pronounced effect on the local stress state and consequently the transformation behavior of embedded SMA wires. Bidaux, Bataillard, Manson, and Gotthard (1993) measured significant differences in dynamic behavior between plain SMA wires and SMA polymer composites. This change in response indicated that only the ends of the embedded wires transformed. Paine and Rogers (1993) reported that process induced residual stresses alter the martensite and austenite start temperatures of SMA wires embedded in an elastomeric composite. Hebda et al. (1995) have also discussed the issue of local residual stresses in regards to manufacturing high quality SMA composites.

Recent investigations by Kline, Jonnalagadda and Sottos (1995) and Jonnalgadda, Kline and Sottos (1997) utilized photoelasticity to investigate the interaction between embedded SMA wires and a polymer matrix. The maximum shear stress induced in the matrix due to actuation of the SMA was correlated with the interfacial bond strength of the SMA/polymer interface. As the level of interfacial adhesion increased,the stresses in the matrix also increased. Sottos, Kline, Qidwai and Lagoudas (1996) used the photoelastic technique to observe the transformation behavior of

embedded SMA wires in polymeric matrix. Due to the specimen geometry, only a qualitative understanding of the composite behavior was obtained. Jonnalagadda, Sottos, Qidwai and Lagoudas (1997) extended this work and examined the transformation behavior of SMA ribbons in a polymeric matrix. The ribbon geometry was ideal for comparison of the experimental data with theoretical predictions.

The current investigation provides a more complete quantitative analysis of the transformation behavior of the embedded SMA ribbon. The evolution of stress during transformation is first measured using the photoelastic technique. A numerical simulation of the embedded SMA ribbon is then carried out using the fully coupled unified thermodynamic constitutive model (1996) based on the formalism of Boyd and Lagoudas (1996). Different constitutive models (Tanaka, 1986, Liang and Rogers, 1992, Boyd and Lagoudas, 1996), are incorporated into the unified model by virtue of selecting different forms of the function which represents the transformation induced strain hardening as predicted by these models. Computational predictions by the polynomial model (Boyd and Lagoudas, 1996) are compared with the experimental stress contours.

2. PHOTOELASTIC STRESS ANALYSIS

2.1 Sample Preparation

Photoelastic samples were fabricated by embedding a single SMA ribbon (55% Ni, 45%Ti) 1.22 mm wide and 0.3 mm thick in a room temperature cure epoxy matrix. A schematic of the sample is shown in Figure 1. The ribbons were annealed at 600°C and then sandblasted in order to maximize the adhesion with the matrix. The transformation temperatures of the ribbons were measured using a differential scanning calorimeter (DSC) and listed in Table 1 along with other relevant material properties. One set of ribbons was subjected to a uniform strain of 1% and then embedded in the epoxy matrix. A second set was embedded without any prestraining in control samples. The control samples were tested with the other samples in order to evaluate the purely thermal stresses due to heating.

Because the presence of an initial residual stress field complicates the identification of photoelastic fringes from SMA actuation, matrix materials requiring an elevated temperature cure were avoided. A room temperature cure epoxy resin, EPON 828 (diglycidyl ether of bisphenol A, Shell) cured with Ancamine T (diethylenetriamine, Air Products) was chosen due to its excellent photoelastic properties and low residual stresses. The two part epoxy was thoroughly mixed, degassed for approximately 30 minutes to remove any air bubbles, and then poured into prepared silicon rubber molds containing a single SMA ribbon. Samples were allowed to cure at room temperature for 10 days. As a consequence of the meniscus that formed around the edge of the samples, it was impossible to pour the sample thinner than about 5 mm. Polishing of the samples was necessary to diminish the thickness and to provide a flat surface for use in the polariscope. The final thickness of the prepared samples was approximately 1.45 mm, while the ribbon thickness was 1.27 mm as shown in Figure 1. A thin layer of epoxy was left between the edge of the embedded ribbon and the polished surface to hinder debonding. Even with careful sample preparation, small debonds approximately 1 mm in length formed at the right and left edges of the sample where the ribbon emerged from the polymer block. These initial debonds

Table 1. Material properties of SMA ribbon in austenitic and martensitic phases.

Property	Austenite	Martensite
E (GPa)*	49.0	10.9
ν*	0.3	0.3
α (x 10^{-6} °C)	12.5	12.5
K (W/ m^{o}C)**	18	8.5
ρ (kg/m^3)**	6450	6450
C_A (MPa/^{o}C)**	–	13.5
C_M (MPa/^{o}C)**	13.5	–
A_f (^{o}C)	–	57
A_s (^{o}C)	–	35
M_s (^{o}C)	21.0	–
M_f (^{o}C)	-12.0	–

*Property values taken from Ditman*et al.* (1991).
**Property values taken from Dye (1990).

did not grow during the subsequent experiments but were critical to include in the modeling.

Relevant properties of the epoxy matrix are listed in Table 2. A disadvantage of using a room temperature cure epoxy is the low glass transition temperature ($T_g = 54$°C). For the EPON 828/Ancamine T epoxy, the value of T_g is lower than the austenite finish temperature measured for the ribbons ($A_f = 57$°C). In order to avoid significant stress relaxation in the matrix, the maximum temperature in the sample must remain below T_g, preventing complete transformation of the ribbon. In the current work, the ribbons are heated to a maximum temperature of about 45°C.

2.2. Heating and Actuation

The shape memory effect was induced by resistive heating of the embedded ribbons. This method provided a repeatable, easily controlled heating method. The temperature profile of the samples was measured by placing a thermocouple on the polished epoxy surface at the midpoint of the sample as shown in Figure 2. The temperature change with time was recorded using a LabView driven data acquisition board. Figure 2 is a plot of the temperature profile during heating of the sample. For a current input of 1.55 A, a steady state temperature of 45°C was achieved in

Table 2. Material properties of epoxy matrix.

E (GPa)	2.5
ν	0.33
α (x 10^{-6} °C)	57.0
K (W/ m^{o}C)	0.18
ρ (kg/m^3)	1350
f_σ (kN/m)	15.1
T_g (^{o}C)	56

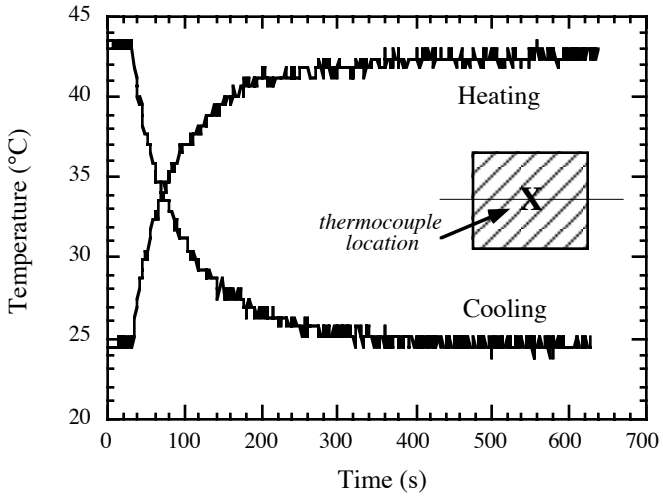

Figure 2. Experimental temperature profile of the SMA ribbon sample.

approximately 200 seconds.

Rather than placing several thermocouples along the ribbon, an infrared camera (Inframetrics 525) was used to ascertain if the sample heated uniformly along its length. Figure 3(a) is typical infrared image of a heated control sample. The relative temperature rise across A-A in isotherm units is plotted in Figure 3(b). Each horizontal line represents a constant temperature, the value of which depends upon the spectral emissivity of the polymer. The length of the sample, L, is indicated by the vertical lines. The temperature remained uniform across the sample length throughout heating. Due to difficulty in obtaining an accurate value for the emmisivity of the polymer matrix, the infrared camera was not used for absolute temperature measurement.

2.3. Apparatus and Experimental Procedure

A polariscope, shown schematically in Figure 4, was constructed using a 1W argon laser as the light source. Since coherent light can create interference fringes, a spinning ground-glass disk was used as a coherency scrambler. Quarter-wave plates were inserted to circularly polarize the light, eliminating the isoclinic fringes from the resulting image. Two lenses were used to expand the diameter of the beam, permitting a larger field of view. The focus of the first lens, with a focal length of 2 cm, was placed at the focus of the second lens, which had a focal length of 20 cm, increasing the thickness of the beam from 2.5 mm to 25 mm. A VCR was connected to a CCD camera to record the development of fringes. A 640 pixel by 480 pixel frame grabber was used to store the recorded images as eight-bit gray scale at discrete time increments of 15 seconds.

The polished SMA ribbon sample was mounted in the polariscope. The exposed edges of the ribbons were connected to a power supply and heated resistively with

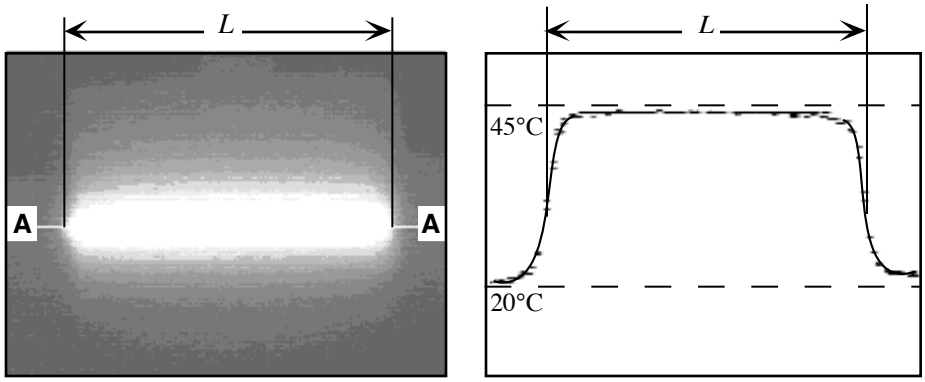

Figure 3. (a) Infrared image of SMA ribbon sample; (b) Temperature profile along sample in isotherm units.

a current of 1.55 A. In order to separate the purely thermal effects, control samples with annealed SMA ribbons were tested first. No discernible fringe development was observed with time indicating that the stresses induced by the thermal load were negligible. Any significant relaxation of the matrix from heating too close to T_g would result in a distorted fringe pattern near the SMA wire. No such distortions were observed during the experiment. The samples with 1% strain were tested next. Photoelastic fringe patterns were acquired before, during and after actuation. The development of photoelastic fringes for consecutive time intervals is shown in Figure5(a). Because the fringe patterns are symmetric, only the left half of the sample is presented. As the amount of actuation increased, the fringes moved radially outward from the ribbon and toward the center of the sample.

2.4. Experimental Stress Analysis

A quantitative two-dimensional photoelastic stress analysis was performed on the images of the SMA/polymer specimen in Figure 5(a). Since the experiments with annealed ribbons indicated that the thermal contribution to stress development was negligible, all of the observed fringe patterns were attributed to the SMA actuation. Accurate determination of the locations of the fringes was made using an image analysis program (Image V1.49 from NIH). The difference between the principal stresses induced in the matrix was then calculated using the stress optic law

$$\sigma_1 - \sigma_2 = \frac{N f_\sigma}{h} \tag{1}$$

where N is the fringe order, h is the thickness of the sample and f_σ is the material fringe value.

The $\sigma_1 - \sigma_2$ contours for the top half of the symmetric photoelastic images are plotted in Figure 5(b) for different time intervals. A stress contour of 5.2 MPa starts out at the edge of the sample and expands horizontally towards the center of the sample while moving out vertically from the ribbon. A second stress contour of 15.6 MPa is first observed at t = 180 sec. With increasing time, this contour moves slightly outward from the ribbon as seen from Figure 5(b) at t = 240 sec. The data provide

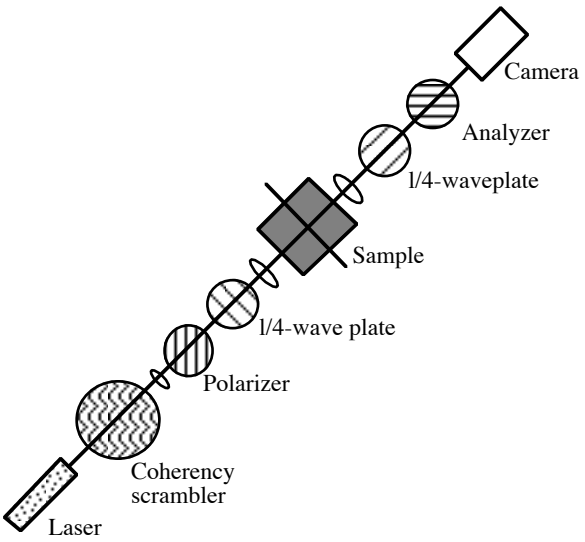

Figure 4. Schematic of circular polariscope.

transient stress profiles for a simple geometry that are ideal for comparison with theoretical models.

3. NUMERICAL SIMULATIONS

The experimental results presented in Section 2.4 are further complemented by numerical simulations using the finite element method to solve the history dependent thermomechanical boundary value problem. The original heat source used in the experiment, and the material constants for SMA and epoxy obtained either from experiments or literature are used as input data. A displacement based finite element method is used to carry out the analysis with the commercial nonlinear finite element code ABAQUS supplemented by a user supplied constitutive subroutine for SMA ribbons. In the following subsections a description of the initial-boundary value problem, field equations and constitutive equations used in the numerical simulations of the experiments is given.

3.1. Boundary and Initial Conditions

Based on the geometry of the experimental setup shown in Figure 1, the 3-D domain schematically shown in Figure 6 (not according to scale) is selected for the numerical simulations. In section 2.4, the photoelastic stress analysis is carried out under the assumption of 2-D stress state. To verify this, a full 3-D problem is considered in the present numerical simulation. The geometry ($\frac{L}{2} \times \frac{L}{2} \times t$) in Figure 6 is the upper left quadrant (ABCDEFGH) of the plate shown in Figure 1, where t is half of the original depth. Using the symmetry with respect to x_1, x_2 and x_3 axes, the planes defined by FBCG, AEFB, and ABCD, are constrained to move in the x_1, x_2, and x_3 directions, respectively. Similarly there is no heat flux through the planes FBCG, AEFB, and ABCD, due to symmetry. The other mechanical boundary conditions are traction free surfaces, while free convection conditions exist where the plate

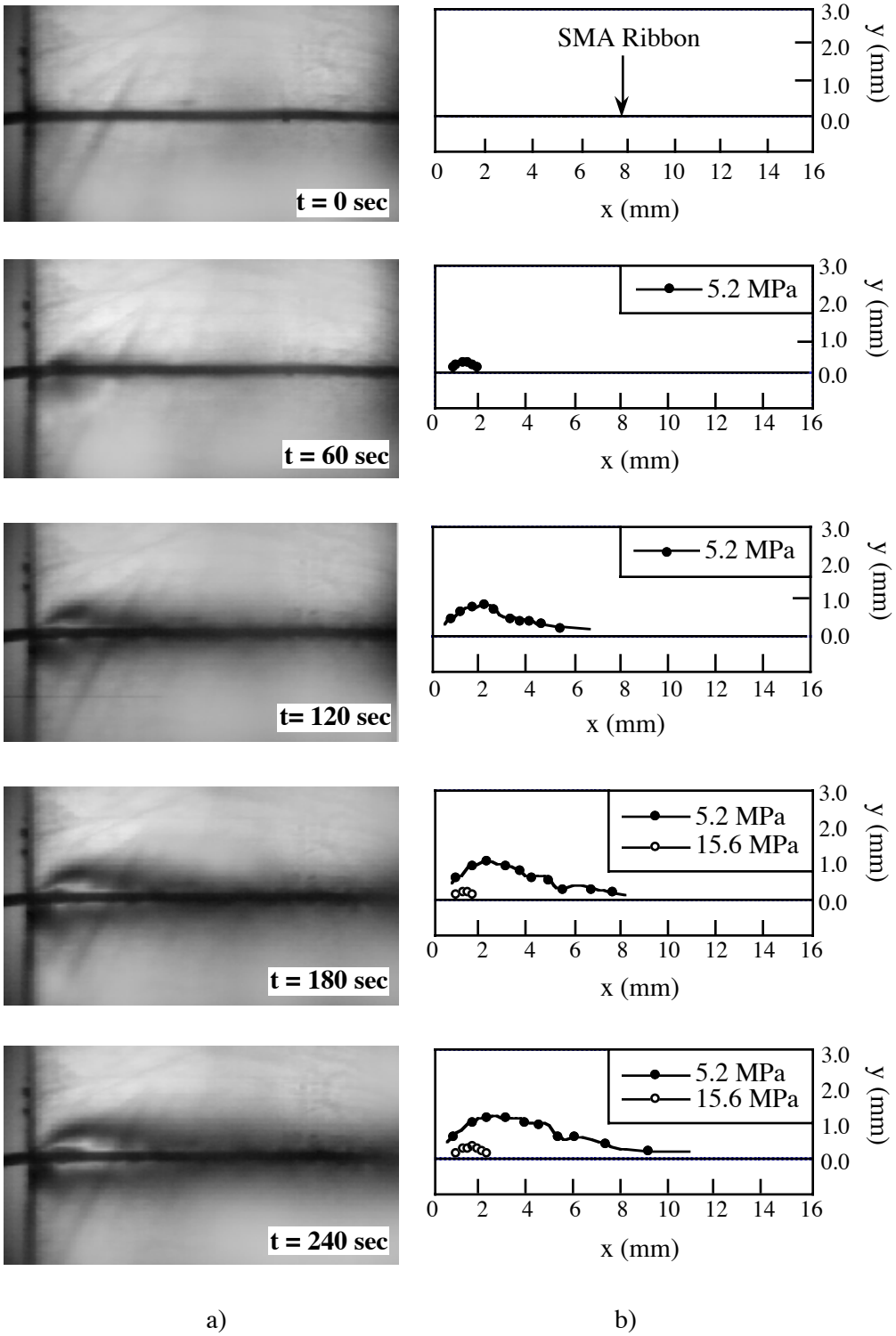

Figure 5. SMA Actuation: (a) Development of photoelastic fringes in SMA ribbon sample; (b) calculated principal stress difference contours for a quarter plate.

is exposed to air on the upper plane EFGH, and the sides DHGC and EADH. The mechanical and thermal boundary conditions imposed on each plane can be mathematically expressed as follows (see Figure 6)

Plane ABCD:

$$\begin{aligned} u_3(x_1, x_2, 0) &= 0, \qquad \sigma_{31} = \sigma_{32} = 0, \\ q_3 &= 0. \end{aligned} \tag{2}$$

Plane EFGH:

$$\begin{aligned} \sigma_{31} &= \sigma_{32} = \sigma_{33} = 0, \\ q_3 &= h(T_s - T_\infty). \end{aligned} \tag{3}$$

Plane FBCG:

$$\begin{aligned} u_1(L, x_2, x_3) &= 0, \qquad \sigma_{12} = \sigma_{13} = 0, \\ q_1 &= 0. \end{aligned} \tag{4}$$

Plane EADH:

$$\begin{aligned} \sigma_{11} &= \sigma_{12} = \sigma_{13} = 0, \\ -q_1 &= h(T_s - T_\infty). \end{aligned} \tag{5}$$

Plane AEFB:

$$\begin{aligned} u_2(x_1, 0, x_3) &= 0, \qquad \sigma_{21} = \sigma_{23} = 0, \\ q_2 &= 0. \end{aligned} \tag{6}$$

Plane DHGC:

$$\begin{aligned} \sigma_{21} &= \sigma_{22} = \sigma_{23} = 0, \\ q_2 &= h(T_s - T_\infty). \end{aligned} \tag{7}$$

In the above equations, q_i $(i = 1, 2, 3)$ is the heat flux in the *ith* direction, h is the free convection coefficient, T_s is the surface temperature, and T_∞ is the ambient temperature. The initial condition to solve the time-dependent heat conduction problem is given by

$$T(x_1, x_2, x_3) = T_0, \tag{8}$$

where T_0 is the initial temperature. Both ambient temperature and initial temperature of the SMA and epoxy are assumed to be the room temperature, i.e.,

$$T_\infty = T_0 = 25.0\ ^0C. \tag{9}$$

Note that the thermomechanical problem is not driven by the thermomechanical initial-boundary conditions, but by the distributed heat source in the SMA ribbon due to resistive (Joule) heating. This heat source will appear in the field equations to be given next.

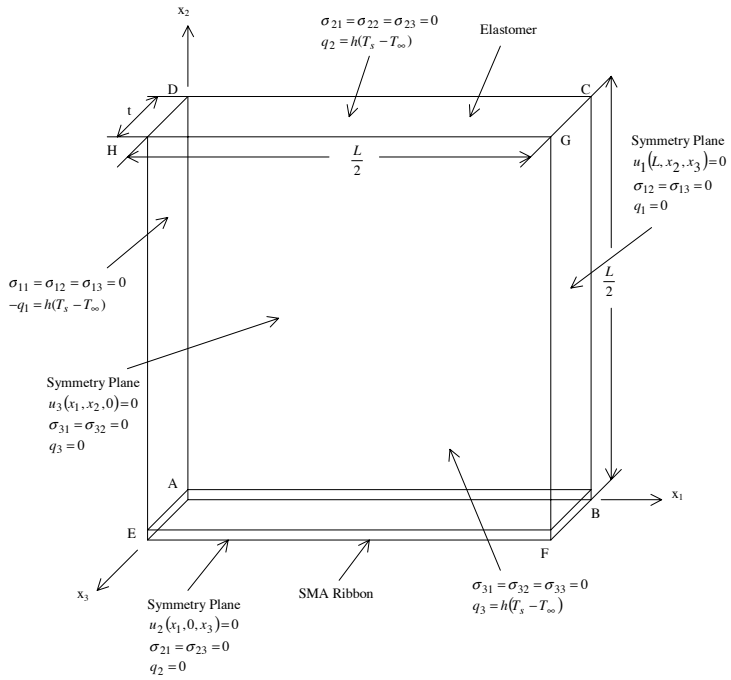

Figure 6. Schematic of the 3-D boundary value problem.

3.2. Field Equations

The present problem is a strongly coupled thermomechanical problem, where the SMA strain hardening behavior is directly influenced by temperature. During a forward phase transformation (austenite to martensite) under adiabatic boundary conditions, an exothermic reaction, the temperature of SMA increases by as much as 70^oC (Bo and Lagoudas, 1998). In that case, the present initial-boundary value problem requires the simultaneous satisfaction of two field equations in both the SMA and epoxy: the equation of equilibrium (balance of linear momentum) assuming body forces and inertial effects are negligible, i.e.,

$$\sigma_{ij,j} = 0, \tag{10}$$

and the heat equation (balance of energy)

$$\rho c\dot{T} = \rho\dot{Q} + \rho\dot{\Omega}. \tag{11}$$

In Eq. (10), σ_{ij} is the Cauchy stress tensor which is assumed to be a function of the infinitesimal total strain tensor, ε_{ij}, the temperature, T, the internal state variable corresponding to the martensitic volume fraction, ξ, and the transformation strain, ε^t_{ij}, for the SMA (see development of SMA constitutive model in Section). For the epoxy, which is assumed to be isotropic elastic (see material properties in Table 2), the stress tensor, σ_{ij}, is only a function of the total strain tensor, ε_{ij}, and the temperature, T. In Eq. (11), ρ and c are the mass density and specific heat of either SMA or epoxy, respectively, and $\rho\dot{\Omega}$ is the two way coupling term between

the thermal and mechanical problem. For elastic materials, $\rho\dot{\Omega}$ is negligible and the two-way thermomechanical coupling reduces to one-way coupling, where only stress is dependent on temperature but not vice versa. The derivation of $\rho\dot{\Omega}$ for SMA is given in Section .

The term $\dot{Q}$ in Eq. (11) is the specific heat input rate due to heat conduction, $-q_{i,i}$, and any applied heat source, r. During the experiment, the only heat source is due to the resistive (Joule) heating of SMA, therefore for SMA

$$\dot{Q} = r - q_{i,i} = \rho_r J^2 + k\nabla^2 T. \tag{12}$$

In the above equation, k is the thermal conductivity assuming Fourier's law of heat conduction, ρ_r is the electrical resistivity of SMA and J is the magnitude of applied electric current per unit area. For epoxy only the last term in Eq. (12) is nonzero, i.e.,

$$\dot{Q} = -q_{i,i} = k\nabla^2 T. \tag{13}$$

Eqs. (10) and (11) form a system of four partial differential equations to be solved in the physical domain defined by the experimental setup shown in Figure 1 for seven unknown fields, i.e., $\sigma_{ij}(x_i, t)$ and $T(x_i, t)$. To reduce the number of unknowns, the stress tensor can be written in terms of the total strain tensor, temperature and the internal state variables $(\varepsilon_{ij}, T, \xi, \varepsilon^t_{ij})$ for SMA and the total strain tensor and temperature for epoxy (ε_{ij}, T), respectively, using constitutive relations. The infinitesimal total strain tensor in turn is related to the deformation field, u_i, by the familiar linearized kinematic relation

$$\varepsilon_{ij} = \frac{1}{2}(u_{i,j} + u_{j,i}), \tag{14}$$

while ξ and ε^t_{ij} will be found by integrating their evolution equations given in the next section. Now the problem is reduced to solving for four unkowns, the deformation field, u_i, and temperature, T, given the above systems of four equations, i.e., Eqs. (10) and (11). The constitutive models used for both materials are described next.

3.3. SMA Thermomechanical Constitutive Model

For the numerical simulation of this problem, the 3-D incremental formulation of the SMA constitutive model, developed by Boyd and Lagoudas (1996) , and Lagoudas, Bo and Qidawi (1996) is used to predict the thermomechanical response of the SMA. A brief description of the constitutive model is given below along with the calibration of material constants for the model in order to relate them to the experimental constants given in Table 1. The two-way coupling term, $\rho\dot{\Omega}$, is also derived here.

The constitutive equations describe the inifinitesimal total strain, ε_{ij}, in terms of stress, σ_{ij}, transformation strain, ε^t_{ij}, temperature, T, and reference temperature, T_o, i.e.,

$$\varepsilon_{ij} = S_{ijkl}\sigma_{kl} + \alpha_{ij}(T - T_0) + \varepsilon^t_{ij}. \tag{15}$$

In the above equation the effective compliance tensor, S_{ijkl}, is defined as the inverse of the effective elastic stiffness tensor, i.e., $S_{ijkl} = (C_{ijkl})^{-1}$, where C_{ijkl} along with the effective thermal expansion coefficient tensor, α_{ij}, are given in terms of the volume fraction of martensite, ξ, by

$$\begin{aligned} C_{ijkl} &= C^A_{ijkl} + \xi(C^M_{ijkl} - C^A_{ijkl}), \\ \alpha_{ij} &= \alpha^A_{ij} + \xi(\alpha^M_{ij} - \alpha^A_{ij}). \end{aligned} \tag{16}$$

For the case in which only phase transformation is considered, the following assumption is introduced to relate the evolution of transformation strains, $\dot{\varepsilon}^t_{ij}$, to the evolution of the martensitic volume fraction, $\dot{\xi}$,

$$\dot{\varepsilon}^t_{ij} = \Lambda_{ij}\dot{\xi}, \tag{17}$$

while the transformation tensor Λ_{ij} is assumed to have the following form

$$\Lambda_{ij} = \begin{cases} \frac{3}{2}H(\bar{\sigma})^{-1}\sigma^{'}_{ij} & \dot{\xi} > 0 \\ H(\bar{\varepsilon}^t)^{-1}\varepsilon^t_{ij} & \dot{\xi} < 0 \end{cases}, \tag{18}$$

where $H = \varepsilon^{t\,max}$ corresponds to the maximum uniaxial transformation strain, and

$$\begin{aligned} \bar{\sigma} &= \sqrt{\frac{3}{2}\sigma^{'}_{ij}\sigma^{'}_{ij}}, \\ \sigma^{'}_{ij} &= \sigma_{ij} - \frac{1}{3}\sigma_{kk}\delta_{ij}, \\ \bar{\varepsilon}^t &= \sqrt{\frac{2}{3}\varepsilon^t_{ij}\varepsilon^t_{ij}}. \end{aligned} \tag{19}$$

The transformation surface equation which defines the thermodynamic force π conjugate to ξ, controls the onset of the forward and reverse phase transformations,

$$\begin{aligned} \pi &= \sigma_{ij}\Lambda_{ij} + \frac{1}{2}\Delta S_{ijkl}\sigma_{ij}\sigma_{kl} + \Delta\alpha_{ij}\sigma_{ij}(T - T_0) + \rho\Delta c\left[(T - T_0) - T\ln\left(\frac{T}{T_0}\right)\right] \\ &\quad + \rho\Delta s_0 T - \frac{\partial f}{\partial \xi} - \rho\Delta u_0 = \pm Y^*. \end{aligned} \tag{20}$$

The terms that are defined with the prefix Δ in Eq. (20) indicate the difference of a quantity between the martensitic (M) and austenitic (A) phases, and they are given by

$$\begin{aligned} \Delta S_{ijkl} &= \frac{\partial S_{ijkl}}{\partial \xi} = -S_{ijpq}\Delta C_{pqmn}S_{mnkl}, \\ \Delta C_{ijkl} &= C^M_{ijkl} - C^A_{ijkl}, \quad \Delta\alpha_{ij} = \alpha^M_{ij} - \alpha^A_{ij}, \quad \Delta c = c^M - c^A, \\ \Delta s_o &= s^M_o - s^A_o, \quad \Delta u_o = u^M_o - u^A_o, \end{aligned} \tag{21}$$

where c, s_o and u_o are the specific heat, specific entropy, and specific energy at a reference state, respectively. The plus sign on the right hand side in Eq. (20) should be used for the forward phase transformation (austenite to martensite), while the minus sign should be used for the reverse phase transformation (martensite to austenite). Note that the material constant Y^* can be interpreted as the threshold value of the transformation surface, π, for the onset of the phase transformation. The evolution of ξ is found by noting that $\dot{\pi} = 0$ during forward and reverse transformation (consistency condition).

The hardening function, $f(\xi)$, describes transformation induced strain hardening in the SMA material and is given by

$$f(\xi) = \begin{cases} \frac{1}{2}\rho b^M\xi^2 + (\mu_1 + \mu_2)\xi & \dot{\xi} > 0 \\ \frac{1}{2}\rho b^A\xi^2 + (\mu_1 - \mu_2)\xi & \dot{\xi} < 0 \end{cases}, \tag{22}$$

where ρb^M and ρb^A are the transformation strain hardening constants. The material constants μ_1 and μ_2 are used to describe the accumulation of elastic strain energy at the onset of the forward phase transformation and to enforce the continuity of $f(\xi)$ at $\xi = 1$, respectively. Further details about the physical interpretation of the equations and material constants introduced above can be obtained from Lagoudas, Bo and Qidwai (1996) .

3.3.1 Fully Stress Coupled Heat Conduction Equation

The total strain-stress constitutive relations in Eq. (15) can be inverted and written in an incremental form as follows

$$\dot{\sigma}_{ij} = C_{ijkl}[\dot{\varepsilon}_{kl} - \alpha_{kl}\dot{T} - Q_{kl}\dot{\xi}], \tag{23}$$

where

$$Q_{ij} = \Delta S_{ijkl}\sigma_{kl} + \Delta\alpha_{ij}(T - T_o) + \Lambda_{ij}. \tag{24}$$

The heat transfer equation (Eq. (11)), which has been obtained by using the first law of thermodynamics, the Legendre transformation between the internal energy, u, and the Gibbs free energy, G, and the definition of G for polycrystalline SMA (Lagoudas, Bo and Qidwai, 1996) can be explicitly written in terms of $\dot{\xi}$ and $\dot{\sigma}_{ij}$, i.e.,

$$\rho c\dot{T} - \rho\dot{Q} = (\pi - T\Delta\alpha_{ij}\sigma_{ij} - \rho\Delta s_o T)\dot{\xi} - T\alpha_{ij}\dot{\sigma}_{ij}. \tag{25}$$

The term on the right hand side of Eq. (25) is $\rho\dot{\Omega}$ (see Eq. (11)) and it provides the two-way coupling between the mechanical and thermal parts. Eqs. (23) and (25) together define the fully coupled stress-temperature system of equations.

To calculate the increment of stress for given strain and temperature increments according to SMA constitutive model, a return mapping integration algorithm proposed by Ortiz and Simo (1986) has been used. For details of the implementation, the work by Lagoudas, Bo and Qidwai (1996) can be consulted.

3.3.2 Determination of Material Constants

For the polycrystalline SMA it can be reasonably assumed that the material is isotropic. In that case, the effective elastic tensor, C_{ijkl}, can be fully represented by the Young's moduli, E^A and E^M, and the Poisson ratios, ν^A and ν^M, where A and M stand for austenite and martensite, respectively. The isotropy also reduces the determination of the effective thermal expansion coefficient tensor, α_{ij}, to the two constants, α^A and α^M. The above constants can be obtained by performing standard tests at low temperature for E^M, α^M, ν^M, and at high temperature for E^A, α^A, ν^A (see Table 1). The maximum uniaxial transformation strain, H, is the residual strain that is retained after the material is fully loaded to the martensitic state at a temperature below A^s and then unloaded completely. The SMA ribbon used in the experiment is given a maximum uniaxial transformation strain of 1%.

For the case of uniaxial tension, the transformation function (Eq. (20)) can be plotted to obtain transformation curves in stress-temperature space. The slopes of these curves (C_A and C_M in Table 1) at zero stress determine the entropy difference $\rho\Delta s_0$ per unit volume between the phases. Lagoudas, Bo and Qidwai (1996) estimated the slope of these curves to be $c_A = c_M = \frac{\rho\Delta s_0}{H}$. Several experiments were conducted at different stress levels by Dye (1990) to obtain the stress-temperature

transformation curves, and the slopes for forward and reverse transformtions were calculated to be 13.5 MPa/^{o}C. In the current model, only the difference in specific heat of both phases, Δc, appears. Many calorimetry experiments show that the specific heat of both phases is almost equal, hence it is assumed that $\Delta c = 0$.

The constant Y^* can be obtained from an isothermal uniaxial pseudo-elasticity test. It is directly correlated to the total hysteresis area enclosed by a stress-strain curve obtained from such an experiment and is given by

$$Y^* = -\frac{1}{2}\rho\Delta s_0(A^{of} - M^{os}) - \frac{1}{4}\rho\Delta s_0(M^{os} - M^{of} - A^{of} + A^{os}). \tag{26}$$

M^{os}, M^{of}, A^{os} and A^{of} are calculated from the strain vs. temperature graph at zero stress, and are given in Table 1. It is not necessary to evaluate $\rho\Delta u_0$ and μ_1 separately, but rather their sum, $\gamma = \rho\Delta u_0 + \mu_1$, since they both contribute to the linear part of the free energy with respect to ξ. γ together with the three constants ρb^A, ρb^M and μ_2 as calculated by Lagoudas, Bo and Qidwai (1996) are given as follows

$$\begin{aligned} \gamma &= \frac{1}{2}\rho\Delta s_0(M^{os} + A^{of}), \\ \rho b^A &= -\rho\Delta s_0(A^{of} - A^{os}), \\ \rho b^M &= -\rho\Delta s_0(M^{os} - M^{of}), \\ \mu_2 &= \frac{1}{4}(\rho b^A - \rho b^M). \end{aligned} \tag{27}$$

The mass density, ρ, and thermal conductivity, k, are also obtained from the work of Dye (1990) and are given in Table 1.

3.4 Epoxy Constitutive Model

Isotropic material behavior is chosen for the constitutive response of the epoxy matrix surrounding the SMA ribbon (see Table 2). This is reasonable because the strains involved are very small (approximately 1% near the ribbon), and as mentioned in section 2.1 the experimental procedure is such that the maximum steady state temperature attained is less than the epoxy glass transition temperature to avoid stress relaxation, thus inelastic effects. Standard tests are performed to obtain the Young's modulus, E, the thermal expansion coefficient, α, and the density, ρ. The values for the poisson's ratio, ν, and thermal conductivity, k, are obtained from the literature.

3.5 Results and Discussion

The boundary and initial conditions discussed in Section , the constitutive response for the SMA ribbon and the epoxy matrix given in Sections and , respectively, and the material constants determined in Section have been used in deriving the results presented in this section. The computations are carried out using the ABAQUS finite element program along with the user supplied subroutine UMAT containing the numerical implementation of the incremental SMA constitutive model. A fully coupled temperature-displacement formulation is used to analyze the problem. In simulating the experimental process, a heat term corresponding to $r(t) = \rho_r J^2 H(t)$ (see Eq. 12) is used as the applied heat source for the coupled thermomechanical problem, where $H(t)$ is the step function. Since a range of values for ρ_r (0.2 $\mu\Omega$-m

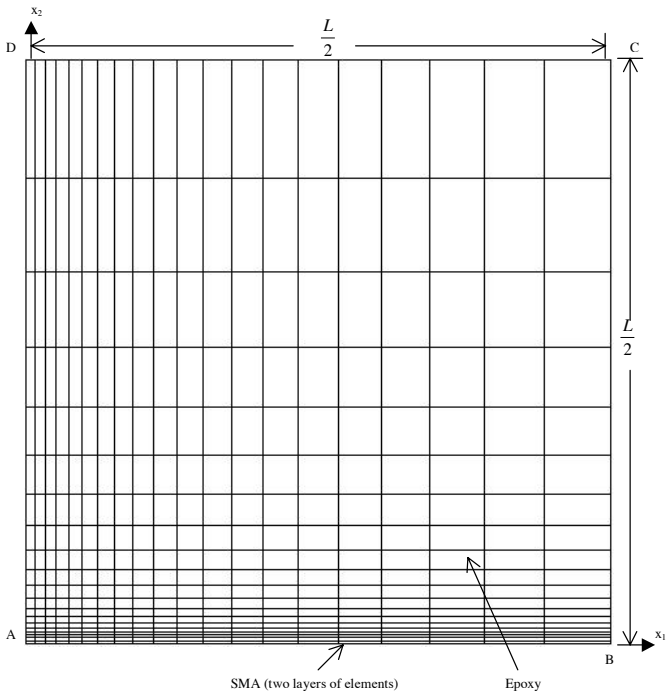

Figure 7. In-plane finite element mesh.

- 0.9 $\mu\Omega$-m) has been reported in the literature (Jackson, Wagner and Wasilewski, 1972) , a suitable value of 0.5 $\mu\Omega$-m is chosen to ensure that the computational steady-state temperature is in agreement with the experimentally measured steady-state temperature in the middle of the specimen (point F in Figure 6). To model the free convection boundary condition, a heat convection coefficient of 10 (W/m^2K) (Incropera and De Witt, 1990) is used. The thin layer of epoxy above and below the SMA ribbon in the polished samples (see Figure 1) is not taken into account in the analysis.

Eight node brick elements are utilized to discretize the problem domain (Figure 7). A convergence study has been performed for 132, 216 and 400 eight node brick finite elements, respectively. All the results presented here are for the FE mesh of 400 elements as shown in Figure 7 (only Plane ABCD of Figure 6 is shown here). Note that only one layer of elements has been introduced in the x_3 direction, because of the small thickness of the specimen.

3.5.1 Effect of Debonded Area on Temperature, Thermodynamic Driving Force and Transformation

To study the effect of debonded area on the stress contour formation, temperature profile and transformation of martensitic volume fraction in the SMA ribbon, simulations are run where the SMA ribbon and the epoxy matrix are fully-bonded and partially debonded. The 1 mm debonded length between the SMA ribbon and the epoxy matrix at the edge of the sample is simulated by defining contact surfaces

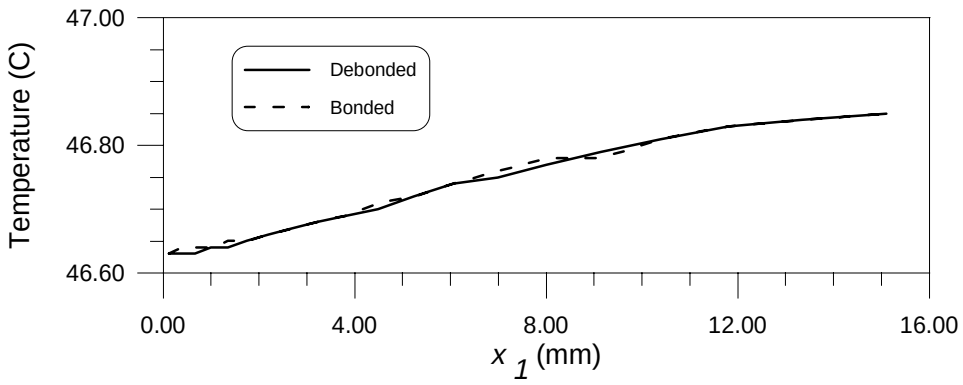

Figure 8. Temperature vs. position along the length of the SMA ribbon for debonded and bonded case.

with Coulomb friction coefficient of $\mu = 0.5$, obtained from SMA fiber-epoxy matrix pull-out experiments (Jonnalagadda, Kline and Sottos, 1997). A large value for the gap conductivity between the contact surfaces is chosen such that it ensures a zero temperature jump across the debonded area.

The simulations are run for a period of 15 minutes and the steady state is attained at approximately 4 minutes for both cases. In Figure 8, the steady state temperature profile versus the position along the ribbon length (x_1-axis) is plotted for fully-bonded and partially debonded cases. The final temperature in the SMA ribbon is found to range from 46.85 ^{o}C at the middle of the ribbon to 46.63 ^{o}C at the free boundary for both cases (steady state). The nearly constant temperature profile along the ribbon length is expected for both cases because of the uniformly distributed heat source along the length of the SMA ribbon and the relatively small influence of the free edge, where a free convection boundary condition is assumed.

In Figure 9, the stress influenced part ($\sigma_{ij}\Lambda_{ij}$) of the thermodynamic phase transformation driving force π (see Eq. (20)) is plotted along the length of the SMA ribbon for both cases. The term $\sigma_{ij}\Lambda_{ij}$ is selected as the stress influenced part of π because the terms $[\frac{1}{2}\Delta S_{ijkl}\sigma_{ij}\sigma_{kl}$ and $\Delta\alpha_{ij}\sigma_{ij}(T - T_0)]$ associated with difference in material properties can be neglected as they are small compared to $\sigma_{ij}\Lambda_{ij}$. Since the temperature profiles are the same for both cases (steady state), the stress influenced part of π is mainly driving the phase transformation. The martensitic volume fraction is plotted along the length of the SMA ribbon for both cases in Figure 10. Taking into account Figure 9, the smaller the stress influenced part ($\sigma_{ij}\Lambda_{ij}$) of π, the lower the magnitude of the martensitic volume fraction, and therefore, the greater the reverse phase transformation. It is further observed in Figure 9 that $\sigma_{ij}\Lambda_{ij}$ is smaller near the free edge for the debonded case than the bonded one. In the debonded case, the stress level in the SMA near the free edge is lower than the fully-bonded case. The presence of debonded area near the edge does not affect the variation of the transformation driving force, temperature, and martensitic volume fraction near the middle of the SMA ribbon at steady state.

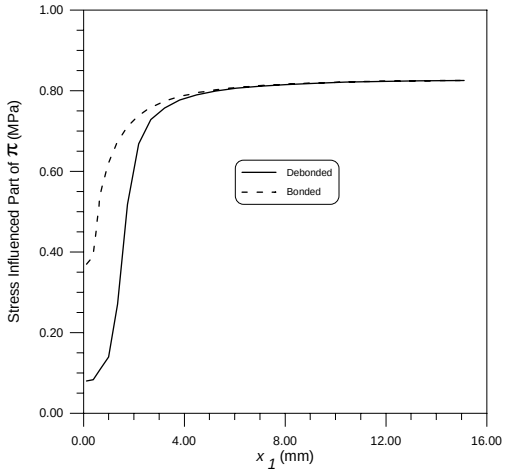

Figure 9. Stress influenced part $\sigma_{ij}\Lambda_{ij}$ of the thermodynamic phase transformation driving force π vs. position along the length of the SMA ribbon for debonded and bonded cases.

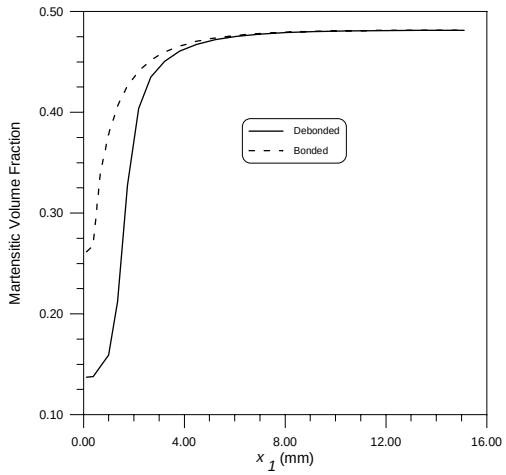

Figure 10. Martensitic volume fraction vs. position along the length of the SMA ribbon for debonded and bonded cases.

3.5.2 Comparison With Experiments

The experimental steady state temperature in Figure 2 is slightly lower than the predicted steady state temperature for the debonded case because the measurements were taken on the surface of the sample (approximately 0.1 mm away from the embedded ribbon). The infrared image in Figure 3 is also a surface measurement and does not have the resolution to detect the small predicted decrease in temperature near the edge of the ribbon.

In the post-processing of the numerical results, the outward normal stress σ_{33} is at least one order of magnitude less than the axial normal stress σ_{11} at all times except during the initial period. The initial similarity in the magnitudes of the normal stresses can be directly attributed to the dominance of volumetric thermal strain over the recovered strain due to phase transformation. However, with time the recovered axial strain, ε_{11}, becomes more dominant (in the order of about 1% compared to 0.01% thermal strain). This indicates that the plane stress assumption used for the photoelastic fringe measurements is valid throughtout the analysis up to the steady state except in the beginning.

In Figures 11-14, contours of Tresca shear stress ($|\sigma_1 - \sigma_2|$ in this case) are plotted for t=60, 120, 180 and 240 seconds. Only two stress levels (5.2 MPa and 15.6 MPa) are used on the contour plots in order to compare the theory with the experiment. The experimental results are given in dotted lines. The computational results match the experiments very well as the time proceeds to the steady state. At 60 seconds, the greatest mismatch occurs (Figure 11). The probable reason is the brief span of time from the initiation of actuation when the SMA has only begun applying compressive stresses on the epoxy. Also, the 15.6 MPa contour predicted at this time is so small, it may be difficult to detect accurately using the current photoelastic set up. Another reason may be the existence of a three-dimensional stress state initially due to relatively strong thermal behavior, instead of the plane stress state as assumed in the experiment.

The emergence of the contour level of 15.6 MPa at 60 and 120 seconds in Figures 10 and 11 is due to the stress concentration at the point where the debonded zone starts. The computational model predictions agree well with the experimental stress contour levels for 120, 180 and 240 seconds, as seen in Figures 12-14. The importance of simulating the debonded area properly is again observed by plotting the computational contours of tresca shear stress at steady state (240 seconds) for the fully bonded case with the experimental results (Figure 15). This shows the shifting of stress concentration from the debonded area towards the free edge, which clearly points out the reason for less transformation in that region than the debonded case for the same temperature and amount of time.

4. CONCLUSIONS

The development of stress due to the actuation of an SMA ribbon embedded in a epoxy matrix was investigated in-situ using photoelastic measurements. Transformation fronts in the composite were observed to move toward the center of the sample and away from the end of the embedded ribbon. The difference in principal stress, $\sigma_1 - \sigma_2$, was calculated at discrete time increments via fringe analysis. Two distinct stress contours with values 5.2 MPa and 15.6 MPa were observed to evolve with time.

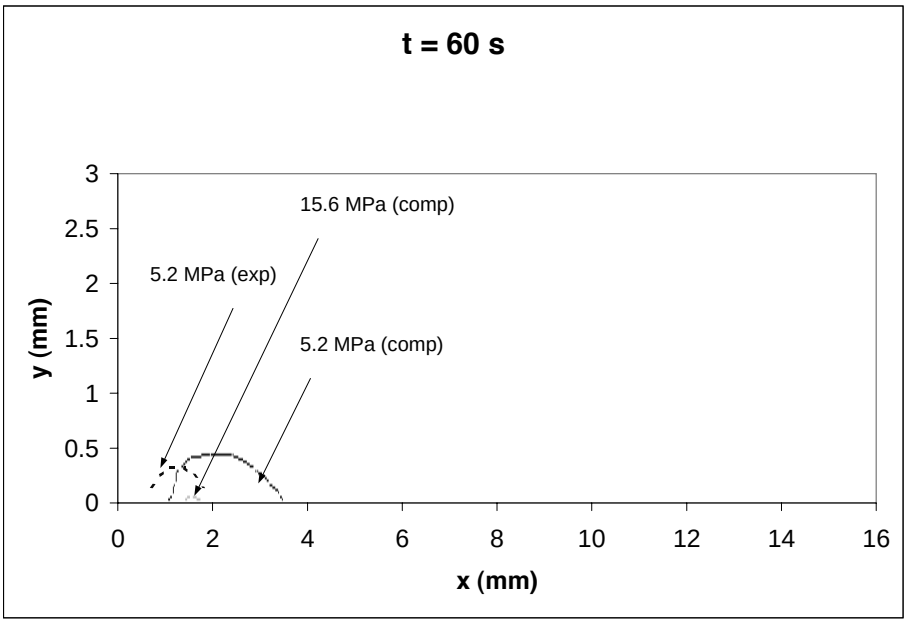

Figure 11. Experimental and computational principal stress difference contours for a quarter plate, t=60 sec.

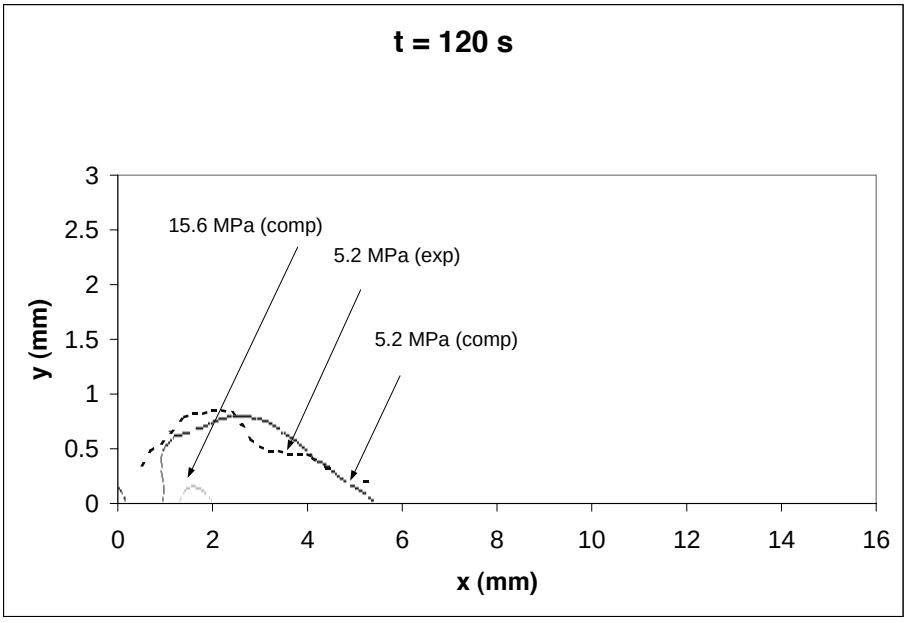

Figure 12. Experimental and computational principal stress difference contours for a quarter plate, t=120 sec.

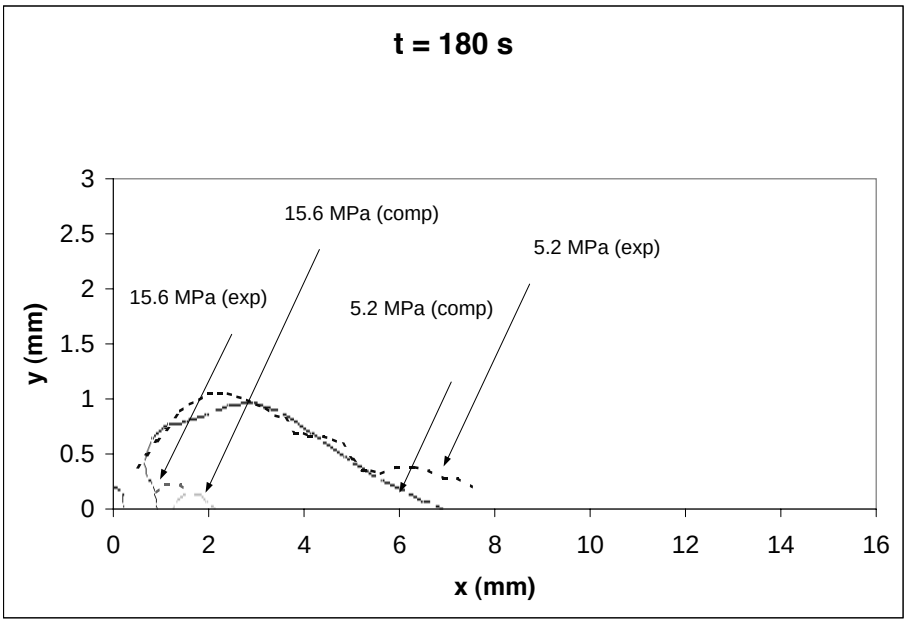

Figure 13. Experimental and computational principal stress difference contours for a quarter plate, t=180 sec.

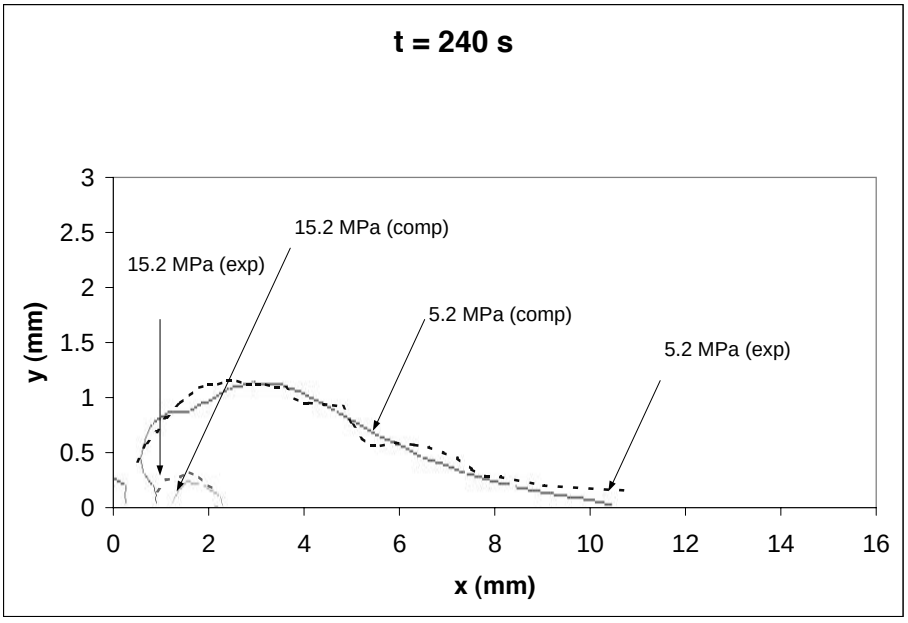

Figure 14. Experimental and computational principal stress difference contours for a quarter plate, t=240 sec.

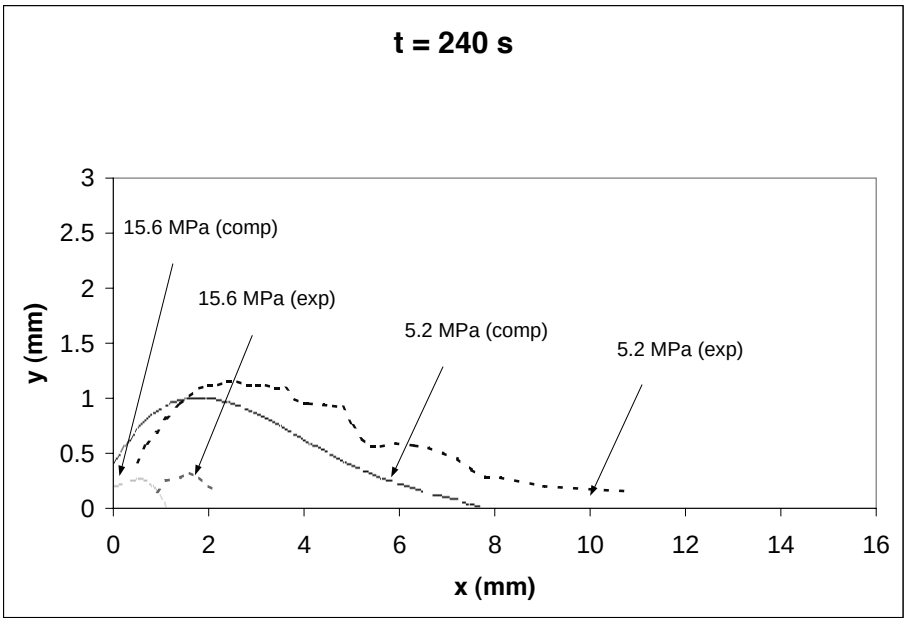

Figure 15. Experimental and computational prinicpal stress difference contours for a quarter plate for the fully bonded case, t=240 sec.

Numerical simulations of the embedded ribbon were carried out using a fully coupled thermomechanical SMA constitutive model for partially debonded and fully-bonded cases. The simulations underscored the critical effect of debonded area on the correct prediction of stress contours and phase tranformation. Absence of a debonded area caused the stress concentration to shift towards the free edge resulting in lesser thermodynamic driving force, and thus lesser transformation near the edge than the fully-bonded case. For the partially debonded case the model reasonably predicted the stress contours of 5.2 MPa and 15.6 MPa throughout the experiment. The initial disparity at 60 seconds between the experimental and numerical stress contour level of 5.2 MPa was due to relatively strong thermal conditions which may favor three-dimensional stress state (due to volumetric thermal effects and small recovered axial strain due to phase transformation) rather than the plane stress assumption used in the photoelastic fringe measurements. At longer times, the model quite accurately predicted the evolution of the stress contours at 120, 180 and 240 seconds.

References

[1] A. Baz and J. Ro. Thermo-dynamic chracteristics of nitinol reinforced composite beams. *Composites Engineering*, 2:527–542, 1992.

[2] J.-E. Bidaux, L. Bataillard, J.-A. Manson, and R. Gotthardt. Phase transformation behavior of thin shape memory alloy wires embedded in a polymer matrix composite. In *Proceedings of 3rd European Conf. on Advanced Materials and Processes*, Paris, France, 1993.

[3] Z. Bo and D. C. Lagoudas. Thermomechanical modeling of polycrystalline smas under cyclic loading, part i: Theoretical derivations. *International Journal of Engineering Science*, 1998. Accepted for publication.

[4] J.G. Boyd and D.C. Lagoudas. A thermodynamic constitutive model for shape memory alloy materials. *International Journal of Plasticity*, 12(86):805–842, 1996.

[5] Z. Chaudry and C. A. Rogers. Response of composite beams to an internal actuator force. In *Proceedings of the 32th Structures, Structural Dynamics and Materials Conference*, number AIAA-91-1166-CP, pages 186–193, 1989.

[6] J. Ditman, S.R. White, and L. Bergman. Tensile testing of nitinol wire. Technical Report UILU ENG 91-0508, University of Illinois, Urbana IL, 1991.

[7] T.E. Dye. An experimental investigation of the behavior of nitinol. Master's thesis, Virginia Tech, Blacksburg, VA, 1990.

[8] D. A. Hebda and S. R. White. Structural behavior of sma composite beams. In *Adaptive Material Systems*, volume AMD-206, pages 111–119. ASME, 1995.

[9] D.A. Hebda, M.E. Whitlock, J.B. Ditman, and S.R. White. Manufacturing of adaptive graphite/epoxy structures with embedded nitinol wires. *Journal of Intelligent Materials and Smart Systems*, 6(2):220–228, 1995.

[10] F. P. Incropera and D. P. DeWitt. John Wiley & Sons, Inc., Singapore, 1990.

[11] C.M. Jackson, H.J. Wagner, and R.J. Wasilewski. 55-nitinol - the allow with a memory: its physical metallurgy, properties, and applications. Technical Report SP-5110, NASA, 1972.

[12] K.D. Jonnalagadda, G.E. Kline, and N.R. Sottos. Local displacements and load transfer in shape memory alloy composites. *Experimental Mechanics*, 37(1):82–90, 1997.

[13] K.D. Jonnalagadda, N.R. Sottos, M.A. Qidwai, and D.C. Lagoudas. Transformation of embedded shape memory alloy ribbons. In *Mathematics and Control in Smart Structures*, volume 3039. SPIE, 1997.

[14] G.E. Kline, K. Jonnalagadda, and N.R. Sottos. Correlating interfacial properties with stress transfer in sma composites. In *Adaptive Material Systems*, volume AMD-206, pages 121–128. ASME, 1995.

[15] D.C. Lagoudas, Z. Bo, and M.A. Qidwai. A unified thermodynamic constitutive model for sma and finite element analysis of active metal matrix composites. *Mechanics of Composite Materials and Structures*, 3:155–179, 1996.

[16] C. Liang, J. Jia, and C. Rogers. Behavior of shape memory alloy reinforced composite plates part ii: Results. In *Proceedings of the 30th Structures, Structural Dynamics and Materials Conference*, number AIAA-89-1331-CP, pages 1504–1513, 1989.

[17] C. Liang and C. A. Rogers. The multi-dimensional constitutive relations of shape memory alloys. *Journal of Engineering Mathematics*, 26:429–443, 1992.

[18] J. Paine and C. Rogers. Characterization of interfacial shear strength between sma actuators and host composite material in adaptive composite material systems. In *Adaptive Structures and Material Systems*, volume ASME AD-35, pages 63–70, 1993.

[19] J.S.N. Paine and C.A. Rogers. The effect of thermoplastic composite processing on the performance of embedded nitinol actuators. *Journal of Thermoplastic Composite Materials*, 4(2):102–122, 1991.

[20] C.A. Rogers. Active vibration and structural control of shape memory alloy hybrid composites: Experimental results. *Journal of the Acoustical Society of America*, 88(6):2803–2811, 1990.

[21] M. Ortizand J.C. Simo. An analysis of a new class of integration algorithms for elastoplastic constitutive relations. *International Journal for Numerical Methods in Engineering*, 23:353–366, 1986.

[22] N.R. Sottos, G.E. Kline, M.A. Qidwai, and D.C. Lagoudas. Analysis of phase transformation fronts in embedded shape memory alloy composites. In *Mathematics and Control in Smart Structures*, volume 2715, pages 25–29. SPIE, 1996.

[23] K. Tanaka. A thermomechanical sketch of shape memory effect: one dimensional tensile behavior. *Res. Mechanica*, 18:251–263, 1986.